Comprehensive Assessment of Transient Stability for Grid-Forming Converters Considering Current Limitations, Inertia and Damping Effects

Jinlei Chen, *Member, IEEE*, Qingyuan Gong, Yawen Zhang, Muhammad Fawad, Sheng Wang, *Member, IEEE*, Chuanyue Li, *Member, IEEE*, and Jun Liang, *Fellow, IEEE*

***Abstract*— This paper presents a quantitative assessment of the transient stability of grid-forming converters, taking into account current limitations, inertia, and damping effects. The contributions are summarized in two main aspects: First, the analysis delves into transient stability under a general voltage sag scenario for a converter subject to current limitations. When the voltage sag surpasses a certain threshold, transient instability becomes a concern, with the severity of this instability being influenced by inertia and damping coefficients within the swing equation. Second, a comprehensive evaluation of these inertia and damping effects is conducted using a model-based phase-portrait approach. This method allows for an accurate assessment of critical clearing time (CCT) and critical clearing angle (CCA) across varying inertia and damping coefficients. Leveraging data obtained from the phase portrait, an artificial neural network (ANN) method is presented to model CCT and CCA accurately. This precise estimation of CCT enables the extension of practical operation time under faults compared to conservative assessments based on equal-area criteria (EAC), thereby fully exploiting the system's low-voltage-ride-through (LVRT) and fault-ride-through (FRT) capabilities. The theoretical transient analysis and estimation method proposed in this paper are validated through PSCAD/EMTDC simulations.**

***Index Terms*—Grid-forming converters, transient stability analysis, current limitation, virtual inertia and damping effects.**

I. Introduction

GRID-FORMING converters play crucial roles in weak power systems, particularly in the context of renewable energy integration and grid stability enhancement. These converters serve as primary sources of grid voltage and frequency regulation, effectively emulating the behavior of traditional synchronous generators [1]-[3]. By dynamically adjusting their output voltage and frequency, grid-forming converters ensure system stability and reliability, even in the presence of fluctuating renewable energy sources [4], [5]. Additionally, these converters facilitate the island-mode operation of renewable energy resources, allowing them to operate independently of the grid or support grid restoration during blackouts [6].

Transient stability is one of the critical aspects of grid-forming converters' performance during large disturbances, such as faults or sudden changes in source or load conditions. Significant disturbances can jeopardize the transient stability of power electronic converters due to abrupt fluctuations in voltage and frequency. Therefore, a thorough transient stability analysis is essential to evaluate the transient stability performance of the system under large disturbances and to develop effective control and protection strategies. The commonly used transient analysis approaches assessing the system transient performance are mainly categorized as three types: equal-rea criterion (EAC) [7], [8], phase portraits [9], [10] and Lyapunov energy function based methods [11], [12]. EAC allows for the determination of transient stability by comparing the decelerating and accelerating areas, without consideration of inertia and damping effects. Phase portraits can also be utilized to illustrate the trajectories of phase angle and frequency, providing an intuitive reflection of stability. Lyapunov functions are designed from the energy perspective, which can also be used to judge the system transient stability according to the critical energy (i.e., stability boundary). However, most previous analyses were conducted based on the conventional power-angle curve and swing equation, completely resembling the behavior of synchronous generators (SGs) [13]. The precision of the results might be compromised as the converter's maximum current is typically restricted to within 1.2 p.u. of its rated value [14]. Hence, the factor of current limitation should be taken into consideration when analyzing transient stability.

To improve the analytical accuracies, impacts of current limitation are then taken into account in transient stability analysis [14]-[19]. In [15], a saturated power-angle curve has been added to illustrate the changes of operating points under current limitations. If the reference of the current controller remains below the maximum value, the operating point will follow the conventional power angle curve. However, once the current reference reaches saturation, the operating point trajectory will transition to the saturated curve. However, only the pure droop controller with d-axis priority current limiting strategy is considered (i.e., the phase angle φ between the

This work was supported by the EPSRC project 'Sustainable Urban Power Supply through Intelligent Control and Enhanced Restoration of AC/DC Networks' under Grant EP/T021985/1. (Corresponding author: Jun Liang).

Jinlei Chen, Qingyuan Gong, Yawen Zhang, Muhammad Fawad, Chuanyue Li and Jun Liang are with the School of Engineering, Cardiff University, CF24 3AA Cardiff, U.K. (e-mail: {chenj111}, {gongq3}, {zhangy408}, {fawadm}, {lic23}, {liangj1}@cardiff.ac.uk).

Sheng Wang is with the School of Engineering, Cardiff University, CF24 3AA Cardiff, U.K., and also with the Compound Semiconductor Applications Catapult, NP108BE Newport, U.K. (e-mail: wangs9@cardiff.ac.uk).

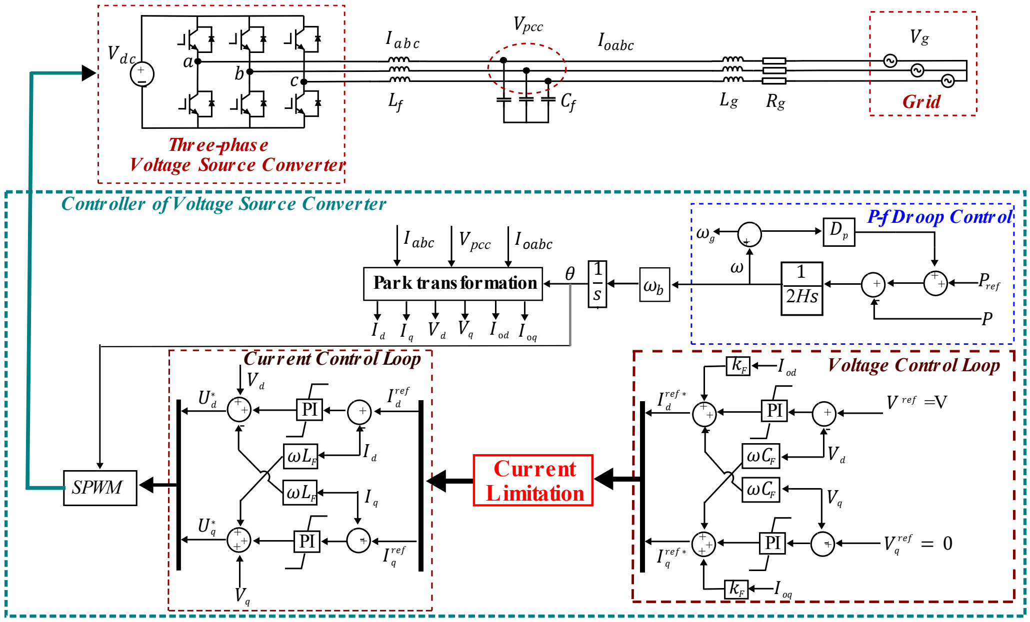

Fig. 1. Grid-forming control schematic.

saturated current reference and the *d*-axis is fixed at zero). Apart from the *d*-axis priority strategy, *q*-axis priority and phase angle priority current limiting strategies have been investigated in [14], [17]-[21]. Based on the comparative study, it is found that the transient stability under fault conditions can be enhanced with increased value of φ. Thus, the *q*-axis priority with $\varphi = \frac{\pi}{2}$ is preferable when considering the transient stability margin only [19]. Although the stability is enhanced, the system cannot switch back to the voltage control mode after the fault is cleared. To this end, the φ is optimally selected in [14] by concurrently considering the stability margin and the ability to switch to the voltage control mode after a fault. Also, the critical clearing time (CCT) and critical clearing angle (CCA) have been theoretically calculated according to the EAC method.

However, previous studies have typically estimated CCT and CCA based on EAC approached [20]. EAC relies on a quasi-static model (i.e., power-angle curve) that does not account for inertia and damping effects. As a result, the maximum allowable fault clearing time derived from EAC tends to be conservative, which may lead to premature system shutdown or protective actions according to the inaccurate estimation. This hinders the complete utilization of low-voltage-ride-through (LVRT) and fault-ride-through (FRT) capabilities and could result in additional economic losses. Furthermore, voltage sag is a primary factor influencing transient stability. Nevertheless, previous studies have typically relied on assuming a fixed voltage sag, which may be insufficient. Analytical results could differ when a more diverse range of voltage sag scenarios is considered. Since inertia and damping significantly contribute to system stability by mitigating rapid changes in frequency and suppressing the amplitude of frequency oscillations, it is crucial to explore the impact of inertia and damping coefficients on transient stability. Concurrently, it is important to consider a generic voltage sag condition.

The contributions of this paper are twofold. Firstly, it explores transient stability in current-limited converters under general voltage sag conditions, employing a quasi-static model to analyze steady-state performance across different voltage sag scenarios. Secondly, phase portraits are leveraged to quantitatively assess the impacts of inertia and damping terms on transient stability. Recognizing the nonlinear relationships among voltage sags, damping, and inertia terms with CCT and CCA, an artificial neural network (ANN)-based method is presented to accurately estimate CCT and CCA, thereby maximizing LVRT and FRT capability utilization (i.e., the maximum allowable operation time under faults can be extended when compared to the conservative results obtained from EAC calculations). The validity of the analysis and estimation method has been confirmed through simulation using PSCAD/EMTDC. It is important to emphasize that all analyses and control strategies are conducted on a per-unit scale. Thus, they can offer valuable guidance applicable to practical systems with identical per-unit parameters, without sacrificing generalizability.

II. Control Structure and Current Limiting Algorithm of the Presented System

In this section, the overall control structure of the grid-forming voltage-source converters (VSCs) are given first. Then, the priority-based current-limiting algorithms are discussed, including *d*-axis priority, *q*-axis priority and phase angle priority based current limiting algorithms.

A. Control Structure of the Presented System

As shown in Fig. 1, a VSC equipped with a grid-forming controller is connected to a three-phase ac grid. There is an LC filter on the converter side, where L_f denotes the filter inductance and C_f represents the filter capacitance. L_g and R_g are the grid-side inductance and resistance. I_{abc}, I_{oabc}, V_{pcc} and V_g denote the converter-side current, the grid-side current, the point of common coupling (PCC) voltage and the grid voltage, respectively. The circuit parameters are given in TABLE I

The virtual synchronous generator (VSG) control is adopted in the grid-forming controller. It consists of a swing-equation based power synchronization controller (i.e., $P-\omega$ droop controller), a reactive power controller (i.e., $Q-V$ droop controller) and an inner cascaded voltage and current controller. In the swing equation, H and D_p are the inertia and damping coefficients, respectively.

TABLE I
PARAMETERS OF THE PRESENTED SYSTEM.

Parameters	Value	p.u.	Parameters	Value	p.u.
Rated ac voltage $\boldsymbol{V_g}$	320 kV	1	Rated Power S_N	1000 MW	1
Grid frequency f	50 Hz	1	Grid-side inductance L_g	65.2 mH	0.2
Inductance of the LC filter $\boldsymbol{L_f}$	48.9 mH	0.15	Capacitance of the LC filter C_f	2 μF	15.15

For the outer control loop, the reference V^{ref} represents the desired ac voltage magnitude, set to 1 p.u. in this paper. The voltage controller's outputs are the dq current references, which are then fed into the typical current controllers. It is noted that the current references are constrained by a current limiter. This limiter restricts the current reference to a preset current vector if the references exceed the saturation value. Section III-A provides a detailed design and considerations for the current limitation. The design of the current and voltage controllers follows the principles of a typical double closed control loop. With the PWM frequency typically normally set at 10 kHz, the current control loop's bandwidth is chosen to be around 500 Hz, fine-tuned using the Bode diagram. The voltage control loop's bandwidth is designed to be 5-10 times lower than that of the current control loop. Given that the power-droop control loop, which is dominant in transient stability dynamics, operates much more slowly, the effects of the voltage and current controller dynamics are omitted in the paper.

The phase diagram for the circuit in Fig. 1 is illustrated in Fig. 2, and the P and Q injected into the PCC are given as

$$P=\frac{V_g V_{pcc}\sin\delta}{X_g} \tag{1}$$

$$Q=\frac{V_{pcc}^2-V_g V_{pcc}\cos\delta}{X_g} \tag{2}$$

where V_g and V_{pcc} are the magnitudes of the grid voltage and PCC voltage, respectively. δ denotes the phase angle between V_g and V_{pcc} . $X_g=\sqrt{\omega^2 L_g^2+R_g^2}$ is the equivalent line impedance (ω is the angular frequency). It is noted that the mathematical equations in the paper are formulated under per-unit scales.

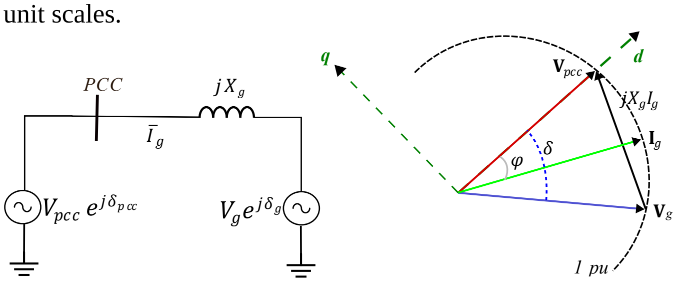

Fig. 2. Phasor diagram of the main circuit.

B. Priority-based Current Limiting Algorithms

There are mainly three types of current limiting control strategies, which were summarized in [17]. The instantaneous limiter is the simplest one to achieve overcurrent protection. However, capacity utilization of the converter is not fully released due to the element-wise saturation function [22]. On the contrary, magnitude limiter and priority-based limiter can ensure a sinusoidal output current and fully utilize the overcurrent capability. Compared with the magnitude limiter, priority-based methods can direct saturated current references to axes at arbitrary angles, which provides more degrees of freedom of controllability. There, the priority-based current-limiting method is adopted in this paper.

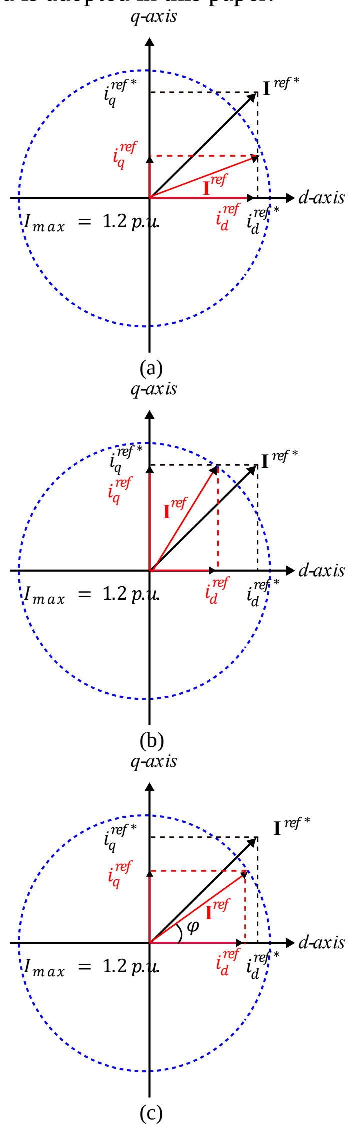

Fig. 3. Priority-based current-limiting approach. (a) d-axis priority. (b) q-axis priority. (c) Phase angle priority.

The priority-based current-limiting approach consists of three categories (see Fig. 3): the d-axis priority, q-axis priority and phase angle priority based current limiting algorithms. It is found that increasing φ can enlarge the stability margin of the system, however, a lager φ may deteriorate the voltage control performance. A suitable φ can be selected according to [14], which is discussed in Section III.

III. Transient Stability Analysis under Different Voltage Sags

In this section, the mathematical model combing the current limitations is first presented. The equilibrium points under different degrees of voltage sags are identified. The analysis reveals a potential risk of transient instability when the voltage falls below a certain threshold.

A. Mathematical Model Considering Saturation of Current Reference

In normal conditions, the current references from the voltage PI controller are not saturated and satisfies:

$$\left\|\mathbf{I}_{dq}^{ref}\right\| = \sqrt{\left(I_d^{ref}\right)^2 + \left(I_q^{ref}\right)^2} < I_{sat} \tag{3}$$

where $\mathbf{I}_{dq}^{ref} = \left[I_d^{ref} \quad I_q^{ref}\right]$ is the vector of current reference, and I_{sat} is the saturation value of the current vector. $\|\mathbf{x}\|$ denotes the magnitude of a vector $\mathbf{x}$. In this condition, the dynamic equation of δ is given as

$$2H\ddot{\delta} = P_{ref} - P - D_p\dot{\delta} = P_{ref} - \frac{V_g V_{pcc}\sin\delta}{X_g} - D_p\dot{\delta} \tag{4}$$

where H and D_p represent the virtual inertia and damping coefficients in the swing equation. P_{ref} is the power reference.

However, during voltage sag or fault conditions, the current reference may reach the maximum value due to the saturation of the voltage PI controller. Thus, there exists $\left\|\mathbf{I}_{dq}^{ref}\right\| \geq I_{sat}$. The dynamic equation of δ in (4) is modified as:

$$2H\ddot{\delta} = P_{ref} - \underbrace{I_{sat}V_g}_{P_{sat}}\cos(\delta - \varphi) - D_p\dot{\delta} \tag{5}$$

where P_{sat} is the maximum power under current saturation.

Take the three-phase fault condition as an example. During and after a fault, the overall trend of the operating point's change is depicted in Fig. 4, with different φ being used (φ_1 in Fig. 4(a) is smaller than φ_2 in Fig. 4(b)). In Fig. 4(a), the power decreases to zero upon an occurrence of a fault at stage 1 ($P_{sat} = 0$). Based on the dynamic equation in (5), δ is increased since the operating points locates at the accelerating area S_A. Once the fault is cleared at stage 2, the operating point moves along the saturated power-angle curve. Although the operating point locates at the decelerating area S_B, δ still increases due to the inertia effects until $\dot{\delta}$ decreases to zero. At stage 3, $\dot{\delta}$ becomes negative, leading to a decrease in δ. Once the operating point reaches the intersection point, it will return to the initial point along the traditional power-angle curve.

In Fig. 4(b), φ_2 is selected larger than φ_1 in Fig. 4(a). As can be seen, S_B' is greater than S_B. Thus, the decelerating area is increased with a larger φ. This implies that more energy can be utilized to facilitate the return of the operating point to its initial state, thereby augmenting transient stability. However, φ should not be excessively large, as it could impair voltage control capability in the post-fault stage [14]. Thus, the optimized φ is obtained in (6) when points "e" and "m" coincide.

$$\varphi_{opt} = \sin^{-1}\left(\frac{P_{ref}}{P_{max}}\right) + \cos^{-1}\left(\frac{P_{ref}}{P_{sat}}\right) \tag{6}$$

where $P_{max} = \frac{V_g V_{pcc}}{X_g}$ is the maximum power without considering the current limitations. Hence, φ_{opt} is adopted in this paper for analysis due to its good balance between the transient stability enhancement and a post-fault voltage control capability.

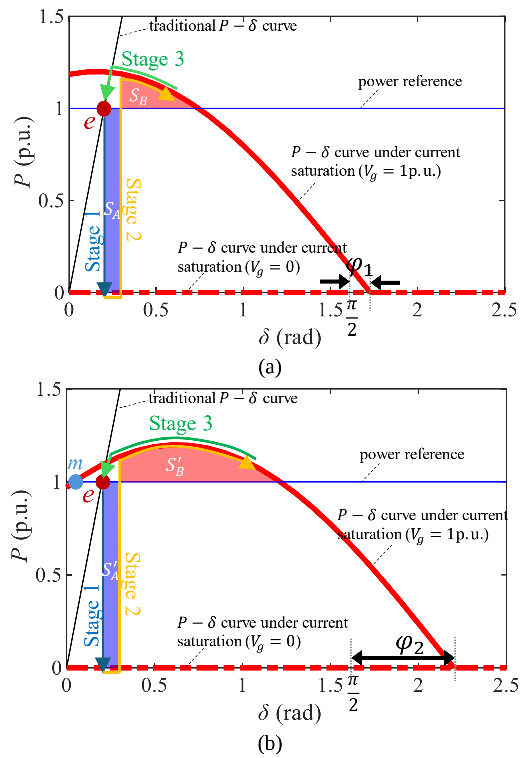

Fig. 4. Trajectories of operating point on $P-\delta$ curve with different φ of $\boldsymbol{I}^{ref}$. (a) $P-\delta$ curve with a smaller φ. (b) $P-\delta$ curve with a larger φ.

The design of the current limitation in Fig. 1 is shown in Fig. 5. The magnitude of the current vector $\left\|\mathbf{I}_{dq}^{ref*}\right\|$ is compared with the saturation value I_{sat}. If $\left\|\mathbf{I}_{dq}^{ref}\right\|$ is greater than I_{sat}, the dq references will be $I_d^{ref} = I_{sat}\cos(\varphi_{opt})$ and $I_q^{ref} = I_{sat}\sin(\varphi_{opt})$, respectively. Otherwise, the current references are equal to the outputs directly obtained from the voltage controller.

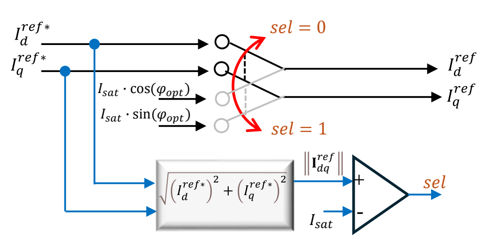

Fig. 5. Diagram of the implementation of the current limitation.

B. Transient Stability Analysis under Different Voltage Sags

If $P_{sat} > P_{ref}$ holds during the voltage sages, equilibrium point exists. Otherwise, equilibrium point does not exist during the voltage sags. Consequently, three conditions may arise. In *Condition 1*, the equilibrium point exists, and the operating point can return to this equilibrium point under a voltage sag. In *Condition 2*, the equilibrium point exists but the operating point may not return to this equilibrium point unless the fault is cleared promptly. In *Condition 3*, the equilibrium point does not exist under $P_{sat} < P_{ref}$, and the fault must be cleared to prevent instability.

1) *Condition 1*: The prerequisite of this condition is $P_{sat} > P_{ref}$. The range of the voltage drop that satisfy $P_{sat} > P_{ref}$ is:

$$P_{sat} = I_{sat} v_g > P_{ref} \\ \Rightarrow v_g > \frac{P_{ref}}{I_{sat}} \tag{7}$$

Thus, the minimum voltage that allows for $P_{sat} > P_{ref}$ is $V_{g\_min} = \frac{P_{ref}}{I_{sat}}$. The operation mechanism is shown in Fig. 6, where the equilibrium point exists, the operating point can return to this equilibrium point after restoration of a voltage sag. Thus, the fault clearing time and fault clearing angle have no influence on the stability.

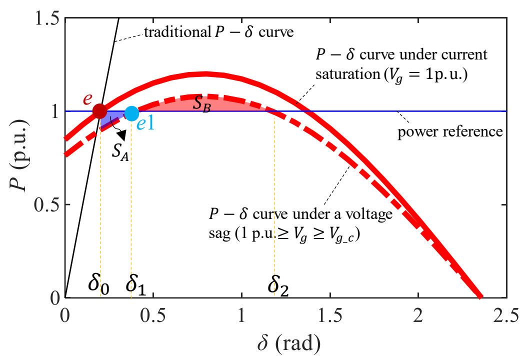

Fig. 6. P–δ curve under condition 1 (1 p.u.≥ $V_g \geq V_{g\_c}$).

In Fig. 6, the conservative boundary of stability during voltage sags can be identified through EAC method, where the critical voltage V_{g_c} can be calculated by considering equal area of S_A and S_B:

$$\int_{\delta_0}^{\delta_1} \left(P_0 - I_{sat} v_g \cos(\delta - \varphi_{opt})\right) d\delta \\ \leq \int_{\delta_1}^{\delta_2} \left(I_{sat} v_g \cos(\delta - \varphi_{opt}) - P_0\right) d\delta \tag{8}$$

Rewriting (8) yields (9):

$$\underbrace{I_{sat} v_g \left(\sin(\delta_2 - \varphi_{opt}) - \sin(\delta_0 - \varphi_{opt})\right)}_{\gamma_1(v_g)} \geq \underbrace{P_0(\delta_2 - \delta_0)}_{\gamma_2(v_g)} \tag{9}$$

where δ_2 and δ_0 are $\delta_2 = \cos^{-1}\left(\frac{P_0}{I_{sat} v_g}\right) + \varphi_{opt}$ and $\delta_0 = \sin^{-1}\left(\frac{P_{ref}}{P_{max}}\right)$. The critical voltage is obtained by comparing the $\gamma_1(v_g)$ and $\gamma_2(v_g)$ in (9). As seen in Fig. 7, the intersection of $\gamma_1(v_g)$ and $\gamma_2(v_g)$ occurs at V_{g_c}=0.87 p.u., which denotes the critical value that allows for the stability during and after a voltage sag.

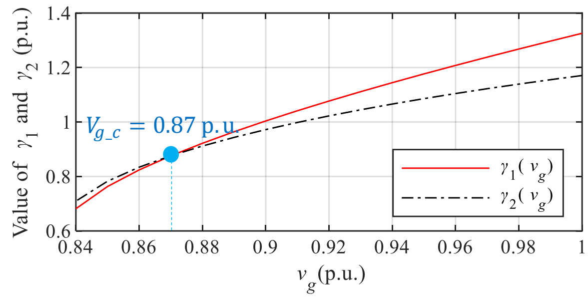

Fig. 7. Solution to (9) by comparing $\gamma_1(v_g)$ and $\gamma_2(v_g)$.

2) *Condition 2*: If v_g locates within the range of $V_{g\_min} < v_g < V_{g\_c}$, S_A ($S_A = S_{A1} + S_{A2}$) is greater than S_B. The operating point cannot automatically return to the equilibrium point if damping effect is omitted, and fault clearance should be considered to avoid transient instability. Assuming the CCA is denoted as δ_{cc} in Fig. 8, it can be obtained by calculating:

$$\int_{\delta_0}^{\delta_{cc}} \left(P_0 - I_{sat} v_g \cos(\delta - \varphi_{opt})\right) d\delta \\ \leq \int_{\delta_{cc}}^{\delta_{max}} \left(I_{sat} V_{g0} \cos(\delta - \varphi_{opt}) - P_0\right) d\delta \tag{10}$$

where V_{g0} is the grid voltage at normal conditions ($V_{g0} = 1$ p.u. is selected), and $\delta_{max} = \cos^{-1}\left(\frac{P_0}{I_{sat} V_{g0}}\right) + \varphi_{opt}$. By solving (10), δ_{cc} is obtained in (11).

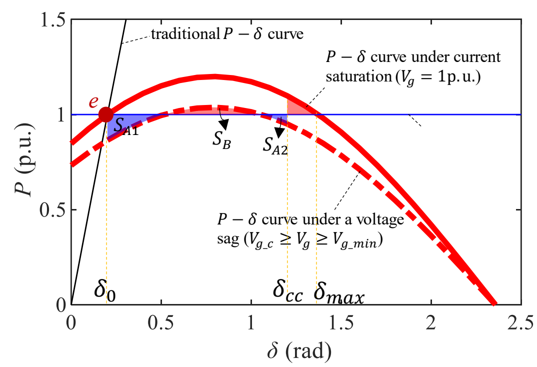

Fig. 8. P–δ curve under condition 2 ($V_{g\_c} \geq V_g \geq V_{g\_min}$).

3) *Condition 3*:

If the voltage further drops, the P_{sat} will be smaller than P_{ref}. In this case, the system is unstable under the voltage sag due to the loss of equilibrium points. Fig. 9 shows the power-angle curve under this condition. To ensure restoration of system stability, the fault must be cleared before the CCA. Given the similar transient behaviors of *Condition 2* and *Condition 3*, the formula of CCA in (11) is also applicable to *Condition 3*. In particular, the CCT under a three-phase short circuit fault (t_{cc}^{sc}) can be calculated by setting v_g as zero. According to the derivation in [23], the t_{cc}^{sc} is given as

$$\delta_{cc} = \sin^{-1}\left(\frac{P_0(\delta_{max} - \delta_0) + I_{sat} v_g \sin(\delta_0 - \varphi_{opt}) - I_{sat} V_{g0} \sin(\delta_{max} - \varphi_{opt})}{I_{sat}(v_g - V_{g0})}\right) + \varphi_{opt} \tag{11}$$

$$t_{cc}^{sc} = \sqrt{\frac{4H(\delta_{cc} - \delta_0)}{\omega_b P_0}} \tag{12}$$

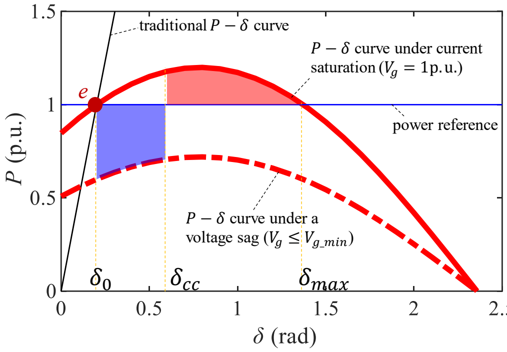

Fig. 9. P–δ curve under condition 3 ($V_g \le V_{g\_min}$).

IV. Assessment of Fault Clearance Considering Inertia and Damping Effects

In this section, transient stability is analyzed based on the phase portrait approach, considering inertia and damping effects. The impact of the inertia and damping effects has been quantitively identified, and an ANN-based date-driven method is presented to accurately estimate CCT and CCA.

A. *Influence of Inertia and Damping Coefficients on Transient Stability*

To quantitively identify the inertia and damping effects, the phase portraits are adopted for analysis. The phase portraits are plotted in MATALB M-Files based on the mathematical model in (1)-(5). The phase portrait under different H and D_p is shown in Fig. 10, where a 0.5 p.u. voltage drop occurs at a certain time. To facilitate comparisons, different clearing angles δ_{cl} nearby the theoretical δ_{cc} in (11) are chosen.

According to the results in Fig. 10, the actual value of CCA (δ_{cc}^{act}) are listed in Table II, and the corresponding actual value of CCT (t_{cc}^{act}) is also recorded at the same time in MATLAB.

TABLE II

CCA and CCT under Different Inertia and Damping Coefficients

D_p (p.u.)	H (s)	δ_{cc}^{act} (rad)	t_{cc}^{act} (s)
0	0.5	0.4882 ($\delta_{cc}^{act} = \delta_{cc}$)	0.0613
20	0.5	1.1375 ($\delta_{cc}^{act} > \delta_{cc}$)	0.1836
20	2.5	0.8299 ($\delta_{cc}^{act} > \delta_{cc}$)	0.2405

As seen in Table II, the actual CCA to ensure the transient stability will be extended when inertia and damping effects are considered. This implies that using the theoretical δ_{cc} in practical applications could result in premature system shutdown or protective actions, although from a stability

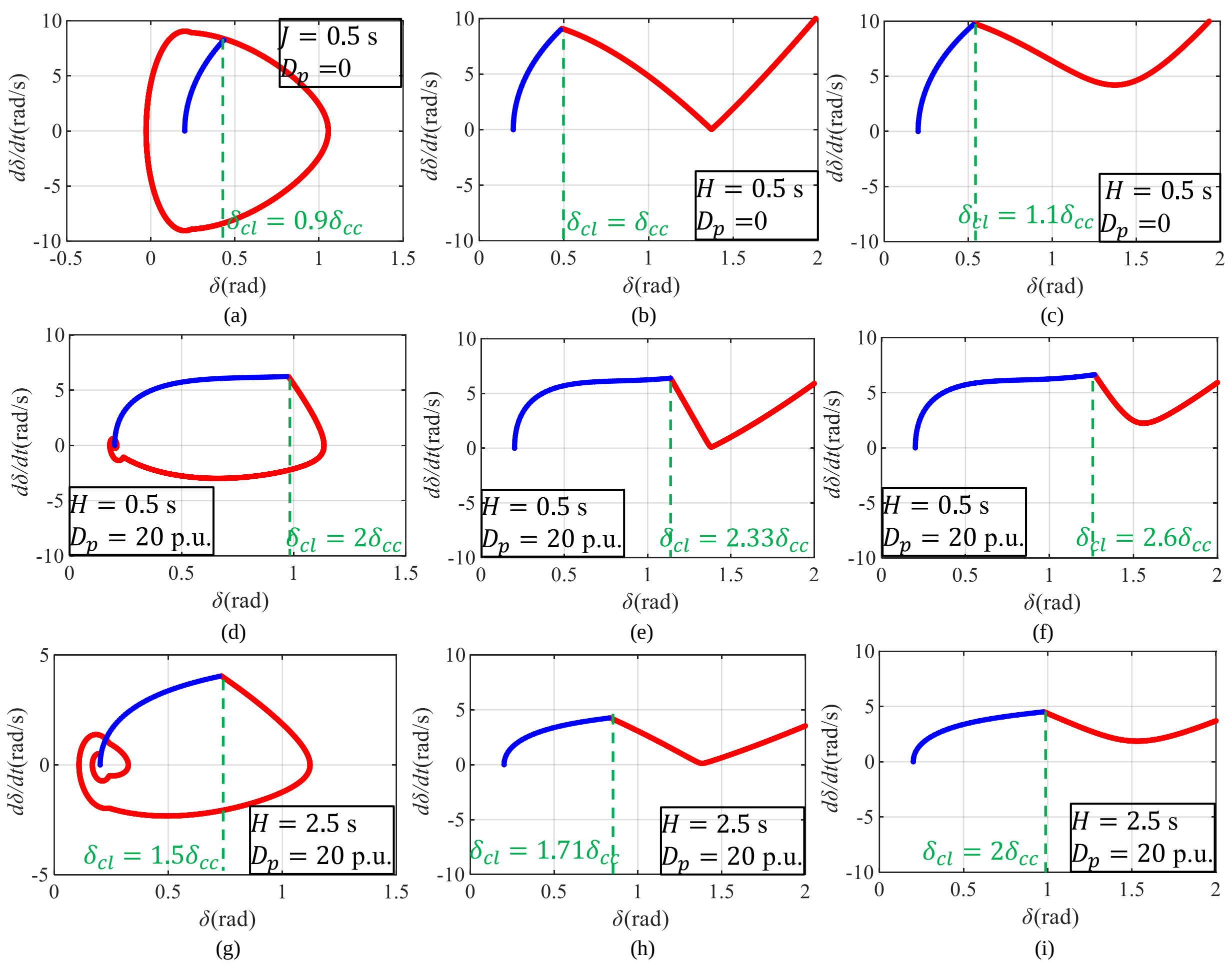

Fig. 10. Phase portrait plots for different values of H and D_p (blue lines represents the trajectories during a voltage sag, and red lines represents the trajectories after the ac voltage is restored).

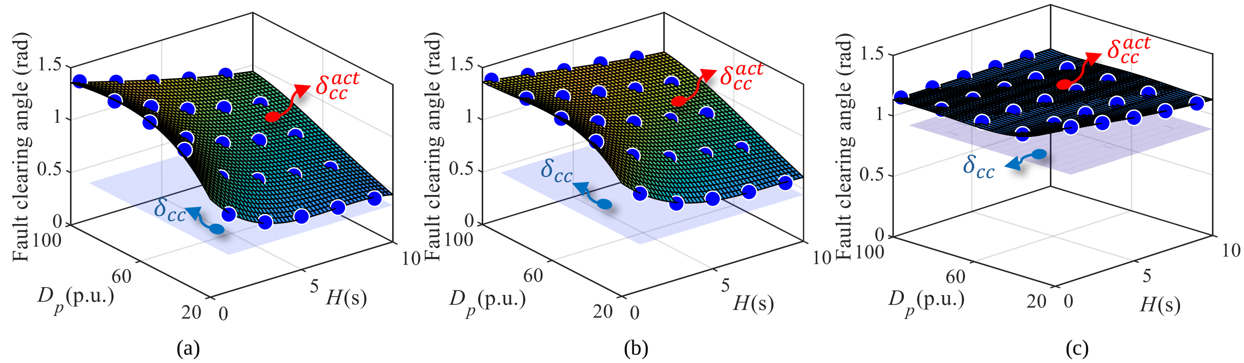

Fig. 11. Fault clearing angles under different voltage drops (the dots are the data obtained from phase portraits, and the surface is the polynomial fitting based on the obtained data). (a) 100% voltage drop. (b) 60% voltage drop. (c) 20% voltage drop.

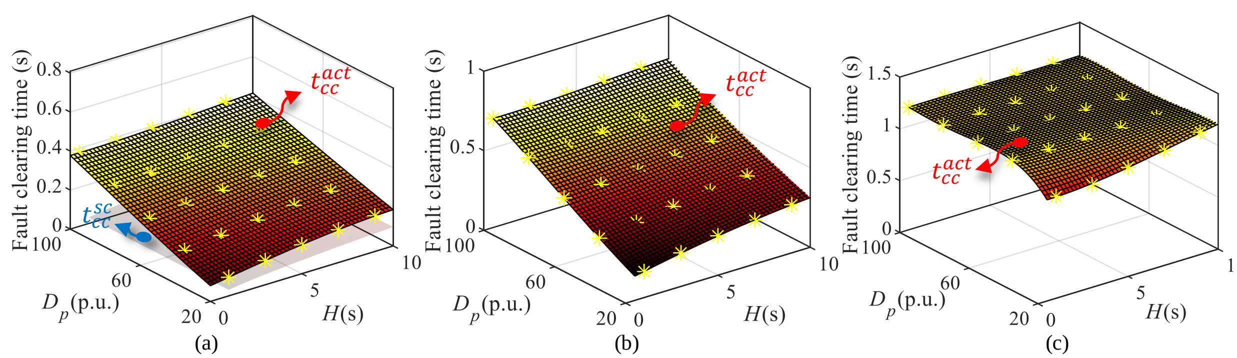

Fig. 12. Fault clearing time corresponding to the fault clearing angle in Fig. 10 under different voltage drops. (a) 100% voltage drop. (b) 60% voltage drop. (c) 20% voltage drop.

perspective, this is a more conservative approach.

A more comprehensive analysis of effects of inertia and damping on CCA and CCT is conducted considering different voltage sags, with results depicted in Fig. 11 and Fig. 12. In Fig. 11, δ_{cc}^{act} obtained from phase portrait analysis is compared with δ_{cc} obtained from the EAC method. The blue dots represent measured data obtained from iterative model runs, which are fitted using a polynomial to generate a three-dimensional surface. The values of D_p and H are chosen within a reasonable range [24], [25]. It is seen that δ_{cc}^{act} is greater than δ_{cc} under all scenarios of voltage sags. In Fig. 11(a) during a 100% voltage sag (i.e., the ac short-circuit fault), δ_{cc}^{act} increases with higher damping, while δ_{cc}^{act} decreases inversely with inertia. This inverse relationship is more pronounced at higher damping values. Similar trends are observed in Fig. 11(b) for a moderate voltage drop. However, the sensitivity of δ_{cc}^{act} to damping and inertia coefficients diminishes with smaller voltage drops (20% voltage drop in Fig. 11(c)).

Fig. 12 illustrates the corresponding t_{cc}^{act} to δ_{cc}^{act} in Fig. 11, showing positive relationships of t_{cc}^{act} with both inertia and damping coefficients. However, these impacts are less pronounced under slight voltage drop conditions. Moreover, the sensitivity of H to t_{cc}^{act} is higher that of D_p (e.g., $\left.\frac{\partial t_{cc}^{act}}{\partial H}\right|_{D_p=60}$=6.8 ms/s and $\left.\frac{\partial t_{cc}^{act}}{\partial D_p}\right|_{H=5}$=3 ms/p.u. are obtained from Fig. 12(a)). This suggests that the inertia coefficient has a greater impact on the CCT compared to the damping coefficient when subjected to the same incremental changes in values.

The trends of δ_{cc}^{act} and t_{cc}^{act} exhibit nonlinear characteristics among voltage sags, inertia and damping coefficients, complicating the creation of a unified polynomial fitting function for estimation. To handle the complexity of modeling the relationship between multiple inputs and outputs, an ANN-based estimation method is introduced in the following section.

B. ANN-based estimation method for CCA and CCT

In Fig. 13, the ANN consists of an input layer, a hidden layer, and an output layer. Three signals—grid voltage, damping, and inertia coefficients—are fed into the input layer. The hidden layer contains N neurons situated between the input and output layers. The output layer consists of 2 neurons, representing the actual CCA and CCT.

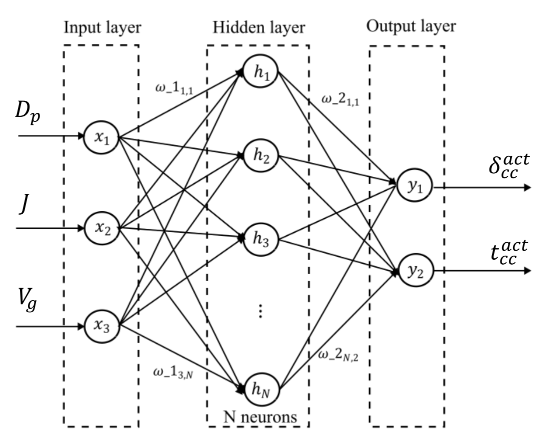

Fig. 13. ANN method for estimating δ_{cc}^{act} and t_{cc}^{act}.

The relationship between the inputs and outputs is given as

$$\delta_{cc}^{act} = f_{ANN}^{CCA}(V,D,J) = \sum_{j=1}^{N}(\omega\_2_{j,1}\,h_j + b\_2_1)$$
$$= \sum_{j=1}^{N}(\omega\_2_{j,1}(sigmoid\left(\sum_{i=1}^{3}\omega\_1_{ij}\,x_i + b\_1_j\right)) + b\_2_1 \quad (13)$$

$$t_{cc}^{act} = f_{ANN}^{CCT}(V,D,J) = \sum_{j=1}^{N}(\omega\_2_{j,2}\,h_j + b\_2_2)$$
$$= \sum_{j=1}^{N}(\omega\_2_{j,2}(sigmoid\left(\sum_{i=1}^{3}\omega\_1_{ij}\,x_i + b\_1_j\right)) + b\_2_2 \quad (14)$$

where ω_1_{ij} is the weight between the i^{th} input-layer neuron and the j^{th} hidden-layer neuron. ω_2_{jm} is the weight between the j^{th} hidden-layer neuron and the m^{th} output-layer neuron. b_1_j is the bias of the hidden layer and b_2_m is the bias of the output layer. x_i and y_i represent the input and output signals, respectively. The sigmoid function serves as the activation function in the hidden layer.

Determining the optimal number of layers and neurons in an ANN is an under-researched topic. For smaller datasets, it is advisable to use fewer layers and neurons, whereas larger datasets benefit from more layers and neurons. In many cases, one or two hidden layers are sufficient, as adding more layers can increase the complexity analytical formulas [26]. The number of neurons in each layer influences the ANN's complexity and its ability to represent patterns effectively. A suitable number of neurons can promote rapid pattern learning. However, using too many neurons can lead to overfitting during training, affecting the network's ability to generalize [27].

V. Simulation Verifications

The simulation test has been conducted in PSCAD/EMTDC to demonstrate the theoretical analysis. The verifications of the system transient stability include three scenarios:

- Verification of inertia and damping effects on transient stability.
- Verification of transient stability under different voltage sags.
- Verification of ANN-based estimation method for predicting δ_{cc}^{act} and t_{cc}^{act}.

A. Influence of Inertia and Damping Coefficients on Transient Stability

Fig. 14 and Fig. 15 show the results under a 50% voltage sag at time 10 s with H=0.5 s and $D_p = 20$ p.u. The fault durations are selected as 230 ms in Fig. 14 and 250 ms in Fig. 15, respectively. It is seen that the current can be effectively limited once the fault occurs. When the low-voltage duration is 230 ms, the system can be successfully restored after the voltage sag is cleared. However, if the low-voltage duration increases to 250 ms, the system becomes unstable even the fault is cleared.

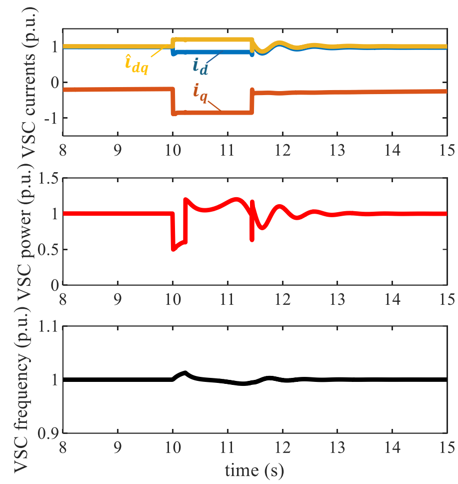

Fig. 14. Results for a fault duration of 230 ms under a 50% voltage sag with H=2.5 s and $D_p = 20$ p.u.

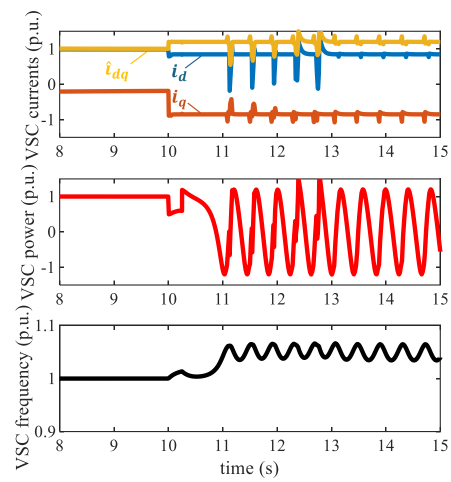

Fig. 15. Results for a fault duration of 250 ms under a 50% voltage sag with H=2.5 s and $D_p = 20$ p.u.

Fig. 16 illustrates the impact of increased inertia and damping on the LVRT capability. In this scenario, the inertia and damping values are doubled compared to those in Fig. 14, while maintaining a low-voltage duration of 250 ms. The findings reveal that increasing both inertia and damping coefficients enhances system transient stability. Nonetheless, the higher inertia depicted in Fig. 16(b) results in larger oscillations during the recovery stage, thereby extending the settling time.

To illustrate the sensitivity of t_{cc}^{act} to H and D_p, a case study is simulated for H=2.5 and $D_p = 22.5$, as shown in Fig. 17. Compared with Fig. 15, it is observed that an incremental change of 2.5 in D_p cannot maintain system stability. However, the same incremental change in H achieves system stability, as depicted in Fig. 16(b), underscoring the stronger relationship between transient stability and the inertia coefficient.

B. Transient stability under different voltage sags

The transient stability under various voltage sag conditions is demonstrated in Figs. 18-20, with simulation studies adopting H=2.5 s and $D_p = 20$ p.u.

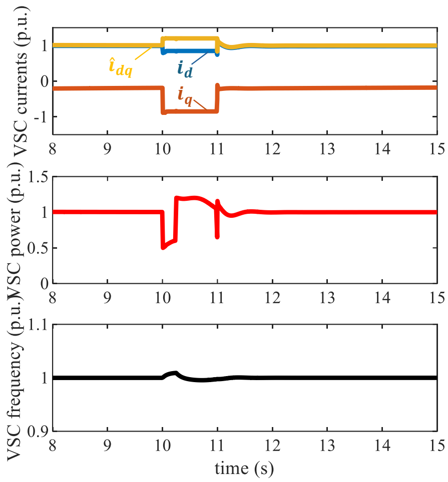

(a)

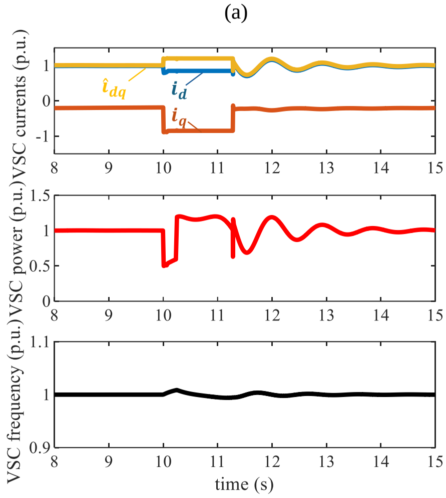

(b)

Fig. 16. Results for a fault duration of 250 ms under a 50% voltage sag with increased inertia and damping. (a) H=2.5 s and D_p = 40 p.u. (b) H=5 s and D_p = 20 p.u.

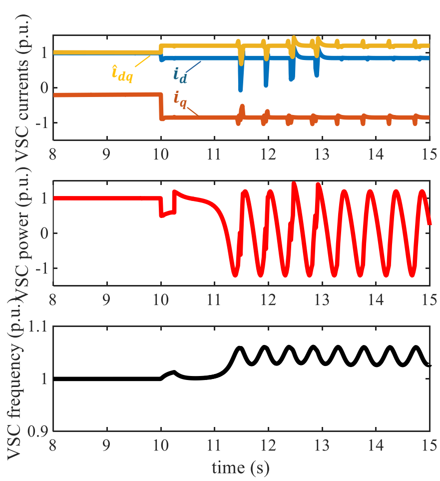

Fig. 17. Results for a fault duration of 250 ms under a 50% voltage sag with H=2.5 s and D_p = 22.5 p.u.

In Fig. 18, a 10% voltage sag occurs at time 10 s with a fault duration of t_{cl}=13 s. Since grid voltage drops by less than the threshold value (0.13 p.u. as shown in Fig. 7), the equilibrium point persists during the sag, ensuring system stability independent of the fault clearing time. However, a 20% voltage drop must be restored within a specified time to prevent instability. As depicted in Fig. 19, the actual critical clearing time t_{cc}^{act} is approximately 1 s, consistent with the findings in Fig. 12(c). In the case of a 100% voltage sag in Fig. 20 (i.e., ac short-circuits fault), t_{cc}^{act} decreases to 110 ms, indicating the fault clearance should be placed considerably earlier with a larger voltage sag.

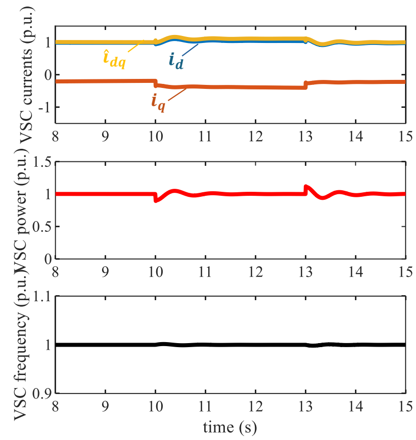

Fig. 18. Results for a 10% voltage sag with existence of equilibrium points.

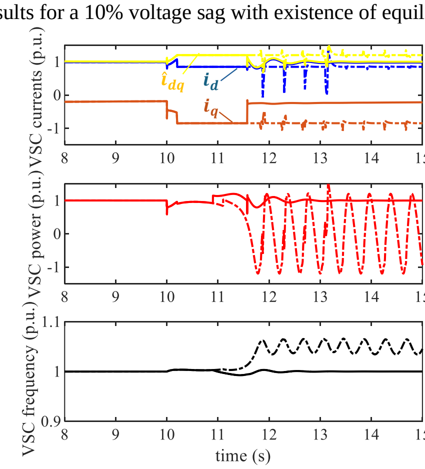

Fig. 19. Results for a 20% voltage sag without existence of equilibrium points (solid line: t_{cl} = 0.9 s; dashed line: t_{cl} = 1.1 s).

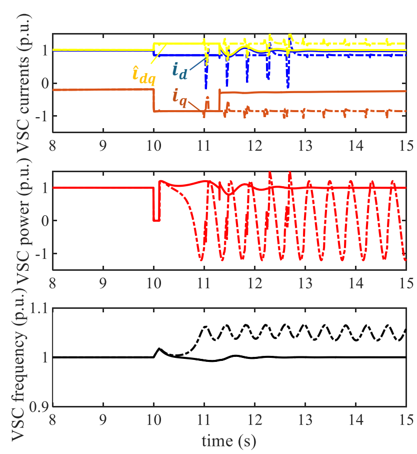

Fig. 20. Results for a 100% voltage sag without existence of equilibrium points (solid line: t_{cl} = 0.11 s; dashed line: t_{cl} = 0.12 s).

C. Performance of ANN-based estimation

Figs. 21-23 depict comparisons of phase portraits under various conditions of voltage sag, inertia, and damping coefficients. The simulation results align closely with the model-based outcomes during voltage sag events, with a minor discrepancy observed in regions where operating points approach equilibrium. This discrepancy is attributed to the dynamics of the voltage control loop. However, the accuracy of δ_{cc}^{act} derived from the model-based phase portrait remains unaffected by these dynamics. Therefore, adopting the model-based phase portrait is reliable for efficiently gathering data used in training ANNs.

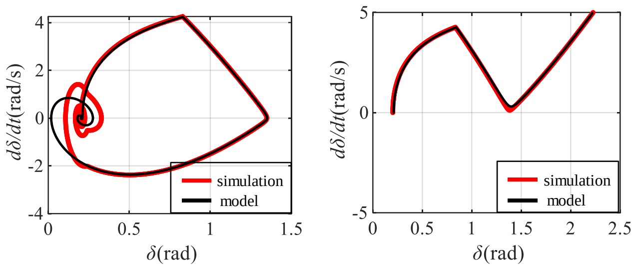

(a) (b)

Fig. 21. Phase portraits for a 50% voltage sag with H=2.5 s and D_p = 20 p.u. (a) Stable operation: t_{cl}=230 ms. (b) Unstable operation: t_{cl}=242 ms.

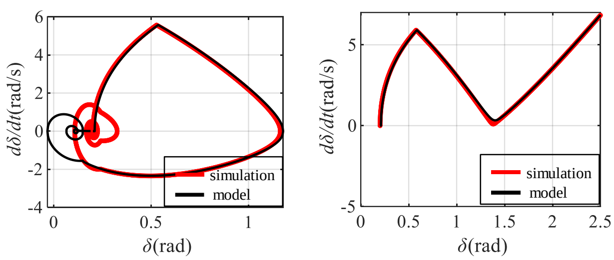

(a) (b)

Fig. 22. Phase portraits for a 100% voltage sag with H=2.5 s and D_p = 20 p.u. (a) Stable operation: t_{cl}=110 ms. (b) Unstable operation: t_{cl}=180 ms.

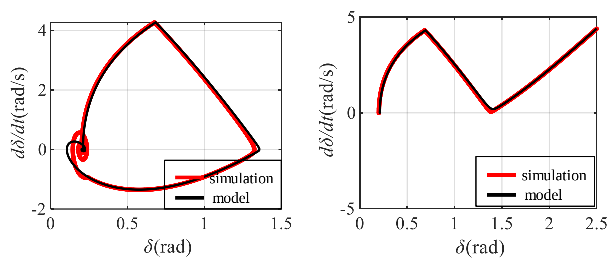

(a) (b)

Fig. 23. Phase portraits for a 100% voltage sag with H=5 s and D_p = 40 p.u. (a) Stable operation: t_{cl}=196 ms. (b) Unstable operation: t_{cl}=199 ms.

The MATLAB Neural Net Fitting toolbox is employed to build and train the ANN model and the weighting coefficients of each layer can be automatically extracted using this MATLAB toolbox. A single hidden layer consisting of 10 neurons is chosen for the network architecture. A dataset consisting of 269 data points is generated using model-based phase portraits and serves as the training data for the ANN model. In this dataset, H ranges from 0.5 s to 10.5 s in steps of 2, D_p ranges from 20 p.u. to 100 p.u. in steps of 20, and the ac voltage ranges from 0 to 0.8 p.u. in steps of 0.1. The training performance is presented in Table III, where the relative root-mean-square error E_{rr_rms} in equation (15) is utilized to quantitatively measure the accuracy of the estimation outcomes relative to the source data. As seen in Table III, the relative root-mean-square errors of the estimated δ_{cc}^{act} and t_{cc}^{act} are 3.09% and 3.54% respectively, which proves the effectiveness of the estimation method.

$$E_{rr\_rms} = \sqrt{\frac{\sum_{i=1}^{N}(y_{si}-y_{ei})^2}{\sum_{i=1}^{N} y_{si}^2}} \tag{15}$$

where y_{si} and y_{ei} are the source and estimated data, respectively. N is the total number of data points.

TABLE III. ANN TRAINING CONFIGURATIONS AND PERFORMANCE

Number of input data	Training data	Validation data	Test data	E_{rr_rms} of δ_{cc}^{act}	E_{rr_rms} of t_{cc}^{act}
269	80%	10%	10%	3.09%	3.54%

Fig. 24 compares the predictions of CCT between the EAC-based and ANN-based methods. The EAC estimates a CCT of 69 ms, whereas the ANN estimates it at 117 ms under a 100% voltage sag. The phase portrait trajectory from the EAC method is enclosed within the trajectory obtained from the ANN method, indicating that the EAC provides a more conservative stability boundary. Thus, the ANN method is a more accurate method for CCT estimation.

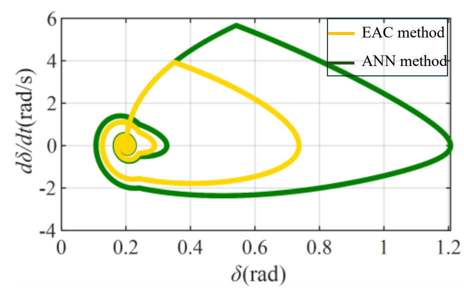

Fig. 24. Trajectories of phase portraits for a 100% voltage sag under the predictions of CCT obtained from EAC-based and ANN-based methods.

D. *Transient stability under different current limitations*

Transient stability is verified under different current limitations, as shown in Fig. 25. The current limitations are set at I_{sat} = 1.2 p.u. and 1.5 p.u., with a fault clearing time of 130 ms.

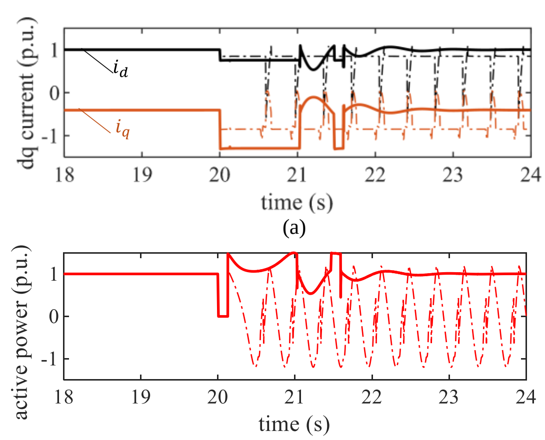

(b)

Fig. 25. Transient stability under different current limitations (solid line: I_{sat} = 1.5 p.u.; dashed line: I_{sat} =1.2 p.u.).

As can be seen, under a 100% voltage sag, the system fails to restore stable operation when I_{sat} is 1.2 p.u. However, when

I_{sat} is increased to 1.5 p.u., stable operation is recovered after fault clearance. This indicates that transient stability can be improved by increasing current limitations.

VI. Conclusions

This paper provides a comprehensive examination of transient stability in grid-forming converters, considering current limitations, as well as the effects of inertia and damping. Utilizing a quasi-static model, the investigation delves into system transient stability considering a general grid voltage sag. It reveals that if voltage drops by less than 0.13 p.u., system stability remains unaffected by damping and inertia, ensuring stability during low-voltage conditions. However, when voltage dips exceed 0.13 p.u., potential transient instability arises, contingent upon the values of damping and inertia outlined in the swing equation. Under such circumstances, prompt fault clearance becomes imperative to avert system instability.

To quantify the influence of damping and inertia on transient stability, model-based phase portraits are utilized. It reveals that actual CCT extends with heightened damping and inertia coefficients. Moreover, the sensitivity of CCT to inertia surpasses its sensitivity to damping. The sensitivities to damping and inertia are more pronounced in scenarios with larger voltage sags compared to minor sag conditions. Leveraging data sourced from the model-based phase portraits, ANN is employed for accurate estimation of CCT and CCA regarding various damping, inertia, and ac voltage sags. The relative root-mean-square errors of estimated CCA and CCT are 3.09% and 3.54% respectively, affirming the efficacy of the estimation approach.

In contrast to conservative assessments derived from conventional EAC methods, the presented assessment method more accurately determines the system's maximum allowable operational duration during low-voltage or fault scenarios, thus maximizing utilization of LVRT and FRT capabilities. Since the analysis is based on a per-unit model, the findings are also applicable to other grid-forming converters, ensuring broad relevance without loss of generality.

References

[1] K. Strunz, K. Almunem, C. Wulkow, M. Kuschke, M. Valescudero, and X. Guillaud, "Enabling 100 % renewable power systems through power electronic grid-forming converter and control: System integration for security, stability, and application to Europe," *Proc. IEEE*, vol. 111, no. 7, pp. 891–915, Jul. 2023.

[2] H. Zhang, W. Xiang, W. Lin and J. Wen, "Grid Forming Converters in Renewable Energy Sources Dominated Power Grid: Control Strategy, Stability, Application, and Challenges," *J. Modern Power Syst. Clean Energy*, vol. 9, no. 6, pp. 1239-1256, November 2021.

[3] K. Mahmoud, P. Astero, P. Peltoniemi and M. Lehtonen, "Promising Grid-Forming VSC Control Schemes Toward Sustainable Power Systems: Comprehensive Review and Perspectives," *IEEE Access*, vol. 10, pp. 130024-130039, 2022.

[4] J. -Y. Park and J. -W. Chang, "Novel Autonomous Control of Grid-Forming DGs to Realize 100% Renewable Energy Grids," *IEEE Trans. Smart Grid*, early access.

[5] M. Andresen, G. De Carne and M. Liserre, "Load-Dependent Active Thermal Control of Grid-Forming Converters," *IEEE Trans. Ind. Appl.*, vol. 56, no. 2, pp. 2078-2086, March-April 2020.

[6] H. N. Villegas Pico and V. Gevorgian, "Blackstart Capability and Survivability of Wind Turbines With Fully Rated Converters," *IEEE Trans. Energy Convers.*, vol. 37, no. 4, pp. 2482-2497, Dec. 2022.

[7] M. G. Taul, X. Wang, P. Davari and F. Blaabjerg, "An Overview of Assessment Methods for Synchronization Stability of Grid-Connected Converters Under Severe Symmetrical Grid Faults," *IEEE Transactions on Power Electron.*, vol. 34, no. 10, pp. 9655-9670, Oct. 2019.

[8] Q. Hu, L. Fu, F. Ma and F. Ji, "Large Signal Synchronizing Instability of PLL-Based VSC Connected to Weak AC Grid," *IEEE Trans. Power Syst.*, vol. 34, no. 4, pp. 3220-3229, July 2019.

[9] A. Hadjileonidas, Y. Li and T. C. Green, "Comparative Analysis of Transient Stability of Grid-Forming and Grid-Following Inverters," in *2022 IEEE Int. Power Electron. Appl. Conf. Expo. (PEAC)*, Guangzhou, Guangdong, China, 2022, pp. 296-301.

[10] D. Pan, X. Wang, F. Liu and R. Shi, "Transient Stability of Voltage-Source Converters With Grid-Forming Control: A Design-Oriented Study," *IEEE J. Emerg. Sel. Topics Power Electron*., vol. 8, no. 2, pp. 1019-1033, June 2020.

[11] F. Andrade, K. Kampouropoulos, L. Romeral, J. C. Vasquez, and J. M. Guerrero, "Study of large-signal stability of an inverter-based generator using a Lyapunov function," in *Proc. IECON*, Dallas, TX, USA, 2014, pp. 1840–1846.

[12] Z. Shuai, C. Shen, X. Liu, Z. Li and Z. J. Shen, "Transient Angle Stability of Virtual Synchronous Generators Using Lyapunov's Direct Method," *IEEE Trans. Smart Grid*, vol. 10, no. 4, pp. 4648-4661, July 2019.

[13] X. Wang, M. G. Taul, H. Wu, Y. Liao, F. Blaabjerg and L. Harnefors, "Grid-Synchronization Stability of Converter-Based Resources—An Overview," *IEEE Open J. Ind. Appl.*, vol. 1, pp. 115-134, 2020.

[14] E. Rokrok, T. Qoria, A. Bruyere, B. Francois and X. Guillaud, "Transient Stability Assessment and Enhancement of Grid-Forming Converters Embedding Current Reference Saturation as Current Limiting Strategy," *IEEE Trans. Power Syst.*, vol. 37, no. 2, pp. 1519-1531, March 2022.

[15] H. Xin, L. Huang, L. Zhang, Z. Wang and J. Hu, "Synchronous Instability Mechanism of P-f Droop-Controlled Voltage Source Converter Caused by Current Saturation," *IEEE Trans. Power Syst.*, vol. 31, no. 6, pp. 5206-5207, Nov. 2016.

[16] L. Huang, H. Xin, Z. Wang, L. Zhang, K. Wu and J. Hu, "Transient Stability Analysis and Control Design of Droop-Controlled Voltage Source Converters Considering Current Limitation," *IEEE Trans. Smart Grid*, vol. 10, no. 1, pp. 578-591, Jan. 2019.

[17] B. Fan, T. Liu, F. Zhao, H. Wu and X. Wang, "A Review of Current-Limiting Control of Grid-Forming Inverters Under Symmetrical Disturbances," *IEEE Open J. Power Electron.*, vol. 3, pp. 955-969, 2022.

[18] K. G. Saffar, S. Driss and F. B. Ajaei, "Impacts of Current Limiting on the Transient Stability of the Virtual Synchronous Generator," *IEEE Trans. Power Electron.*, vol. 38, no. 2, pp. 1509-1521, Feb. 2023.

[19] J. Ji, L. Yang, J. Shi and H. Yang, "Transient Stability Analysis of Virtual Synchronous Generator Considering Current Limitation," in *2023 6th Int. Conf. Energy Elec. Power Eng. (CEEPE)*, Guangzhou, China, 2023, pp. 1306-1311.

[20] A. R. Sobbouhia and A. Vahedi, "Transient stability prediction of power system: A review on methods, classification and considerations," *Elect. Power Syst. Res.*, vol. 190, Jan. 2021, Art. no. 106853.

[21] L. Huang *et al*., "A Virtual Synchronous Control for Voltage-Source Converters Utilizing Dynamics of DC-Link Capacitor to Realize Self-Synchronization," *IEEE J. Emerg. Sel. Topics Power Electron.*, vol. 5, no. 4, pp. 1565-1577, Dec. 2017.

[22] T. Li, Y. Li, X. Chen, S. Li, and W. Zhang, "Research on AC microgrid with current-limiting ability using power-state equation and improved Lyapunov-function method," *IEEE J. Emerg. Sel. Topics Power Electron.*, vol. 9, no. 6, pp. 7306–7319, Dec. 2021.

[23] T. Qoria, F. Gruson, F. Colas, G. Denis, T. Prevost and X. Guillaud, "Critical Clearing Time Determination and Enhancement of Grid-Forming Converters Embedding Virtual Impedance as Current Limitation Algorithm," *IEEE J. Emerg. Sel. Topics Power Electron.*, vol. 8, no. 2, pp. 1050-1061, June 2020.

[24] J. Chen et al., "Demonstration of converter control interactions in MMC-HVDC systems," *Electronics*, vol. 11, no. 2, 2022.

[25] J. Alipoor, Y. Miura and T. Ise, "Power System Stabilization Using Virtual Synchronous Generator With Alternating Moment of Inertia," *IEEE J. Emerg. Sel. Topics Power Electron.*, vol. 3, no. 2, pp. 451-458, June 2015.

[26] P. Yang, W. Ming, J. Liang, I. Lüdtke, S. Berry and K. Floros, "Hybrid Data-Driven Modeling Methodology for Fast and Accurate Transient Simulation of SiC MOSFETs," *IEEE Trans. Power Electron.*, vol. 37, no. 1, pp. 440-451, Jan. 2022.

[27] Y. Liu, J. A. Starzyk, and Z. Zhu, "Optimized approximation algorithm in neural networks without overfitting," *IEEE Trans. Neural Netw*., vol. 19, no. 6, pp. 983–995, Jun. 2008.

Jinlei Chen (M'24) received the B.Eng. and M.Eng. Degrees in automation from Shandong University, Jinan, China, in 2015 and 2018, respectively, and the Ph.D. degree in electrical engineering with Cardiff University, Cardiff, U.K, in 2023. He was a Research Assistant with Cardiff University, Cardiff, U.K. from 2018 to 2023, and a visiting Research Fellow with Compound Semiconductor Applications (CSA) Catapult, U.K. from 2022 to 2023. He has been a Research Associate with Cardiff University, Cardiff, U.K. since 2023. His research interests include control of medium-voltage dc power converters and modeling of compound semiconductor devices.

Qingyuan Gong received his B.Eng. degree in Electrical Information Engineering from Zhejiang University, Hangzhou, China, in 2017, and M.Sc. degrees in Electrical Engineering from Imperial College London, U.K., and Zhejiang University, in 2018 and 2020, respectively. He is currently pursuing a Ph.D. in Electrical Engineering at Cardiff University, U.K. His research interests include power system stability and control, and power electronics.

Yawen Zhang received her bachelor's degree on from Zhengzhou University in 2016. She then completed her master's degree at Wuhan University between 2016 and 2018. Currently, she is pursuing a PhD at Cardiff University, focusing on grid-forming stability and analysis.

Muhammad Fawad received the B.E. and M.E. degrees in Electrical Engineering (Power Systems) from Sukkur IBA University, Sukkur, Pakistan, in 2018 and 2022, respectively. He is currently pursuing the Ph.D. degree in Engineering at Cardiff University, Cardiff, U.K., under the Marie Curie Early-Stage Researcher program. He served as a Lab Engineer at Sukkur IBA University from Dec 2018 to Sep 2023. His research interests include power systems, HVDC grids, grid-forming converters, and renewable energy integration.

Sheng Wang (M'17) received the Ph.D. degree from Cardiff University, in 2016. He has been a Lecturer with the School of Engineering, Cardiff University since 2020. He is the Vice-Chair of the IEEE Power Electronics Society UK and Ireland Chapter. He is also a Research Fellow at Compound Semiconductor Applications (CSA) Catapult. His current research interests include active gate drivers, power electronics devices, wide bandgap semiconductors, and the control and protection of HVDC and MVDC.

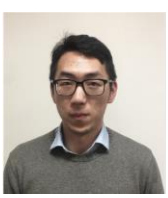

Chuanyue Li (M'17) received dual B.Eng. degrees from Cardiff University, UK, and North China Electric Power University, China, in 2013, followed by a Ph.D. from Cardiff University in 2017. In 2018, he worked as a postdoctoral researcher at the Laboratory of Electrical Engineering and Power Electronics (L2EP) in Lille, France. He is currently a Research Associate at the School of Engineering, Cardiff University, Wales, UK. Since 2023, he has led two industrial projects as the Principal Investigator (PI), with a combined value of approximately £750k. His research interests focus on the stability and control of power-electronics-based power systems.

Jun Liang (M'02-SM'12-F'24) received the B.Sc. degree from Huazhong University of Science and Technology, Wuhan China in 1992, and the M.Sc. and Ph.D. degrees from China Electric Power Research Institute, Beijing China in 1995 and 1998 respectively. From 1998 to 2001, he was a Senior Engineer with China Electric Power Research Institute. From 2001 to 2005, he was a Research Associate at Imperial College, London, UK. From 2005 to 2007, he was a Senior Lecturer at the University of Glamorgan, Wales UK. Currently, he is a Professor at the School of Engineering, Cardiff University, Wales UK. His research interests include DC technologies, power electronics, power system stability control, and renewable power generation.